Surface-acoustic-wave-based Ammonia Gas Sensors Using MoS$_2$/SiO$_2$ Composites

Chan-Yu Chung,[1] Ying-Chung Chen,[1,2] Feng-Renn Juang,[1] and Kuo-Sheng Kao[3*]

[1]Department of Electrical Engineering, National Sun Yat-sen University, Kaohsiung 80424, Taiwan
[2]College of Semiconductor and Advanced Technology Research, National Sun Yat-sen University, Kaohsiung 80424, Taiwan
[3]Department of Computer and Communication, SHU-TE University, Kaohsiung 82445, Taiwan

In this study, delay line surface acoustic wave devices were prepared using a 128° Y-cut LiNbO$_3$ piezoelectric substrate. Pure MoS$_2$ and composite materials of MoS$_2$ and SiO$_2$ with various morphologies were sprayed to form sensitive layers. By adjusting the amount of NH$_4$OH catalyst in the precursors, the particle sizes of SiO$_2$ nanospheres were successfully controlled at 70, 200, and 300 nm by the sol-gel method. SiO$_2$ nanospheres were then added to the precursor for preparing rosette-shaped MoS$_2$, and nanocomposites were synthesized by the hydrothermal method. As a result, two types of composite material were obtained, namely, the S–M structure and the M–S structure. As ammonia gas sensors, the results showed that all the sensors exhibited negative frequency shifts as the NH$_3$ gas concentration increased. Surface area and pore size distribution analyzer (BET) analysis showed that the highest specific surface area of 115.57 m²/g occurred on the S–M structural composite material. The sensor using the S–M structural composite material has a sensitivity of 1932 Hz/ppm to NH$_3$ gas. The sensing linearity R-squared value is approximately 0.99, with continuous dynamic sensing at NH$_3$ gas concentrations of 5–50 ppm. Finally, we revealed that decorating MoS$_2$ with SiO$_2$ nanospheres can improve the adsorption of ammonia molecules and significantly enhance sensitivity.

1. Introduction

Ammonia (NH$_3$) comes primarily from industrial manufacturing processes. It can react with nitrogen oxides (NO$_X$), sulfur oxides (SO$_X$), and water molecules (H$_2$O) in air to form ammonium salts. It is the main source of the major pollutants and PM$_{2.5}$ in haze.[1] The U.S. Occupational Safety and Health Administration (OSHA) has declared that the average ammonia exposure limits for human workplaces are 35 ppm for 15 min and 25 ppm for 8 h.[2] If a human inhales violently high concentrations of NH$_3$, it will cause tears, coughing, difficulty in breathing and other symptoms, and even death.[3] In addition, in the biomedical field, the ammonia concentration in human exhalation is used to determine the possibility of kidney

disease. The ammonia concentration in the breath of healthy people is about 960 ppb, while it is about 4880 ppb in the breath of patients with kidney disease.[4,5]

At present, semiconductor oxides are mostly used as gas sensors. They have the advantages of low cost and simple operation, but there are still some shortcomings that need to be improved. For example, high operating temperatures are required to achieve excellent performance,[6,7] which will lead to high power consumption, hindering wide application and integration in the Internet of Things.[8] Therefore, it is highly beneficial to study high-performance gas sensors that can operate at room temperature and continuously monitor harsh conditions and environments. In this study, we use a delay line surface acoustic wave (SAW) device as the main structure of our ammonia sensor, and rosette spherical molybdenum disulfide (MoS_2) and molybdenum disulfide/silicon dioxide (MoS_2/SiO_2) composite materials are used for sensing layers. SAW devices can be used in gas sensors to measure trace concentrations with high sensitivity and fast response at room temperature.[9] In addition, the electrical signal generated by the SAW device can support wireless sensing and has excellent electrical signal.[10]

SAW devices are mainly composed of two sets of interdigital transducers (IDTs). By applying electrical signals to the input IDTs, the acoustic waves will be generated through the inverse piezoelectric effect and propagate through the delay line area on the surface of the device. At the output IDTs, the acoustic waves will be converted into electrical signals through the positive piezoelectric effect. During the transmission process of the SAW device, the delay line area is coated with nanomaterial to form a sensitive layer that adsorbs gas molecules, causing physical changes and thereby changing the center frequency of the SAW sensor.[11]

MoS_2 has a layered crystal structure in which molybdenum atoms and sulfur atoms are covalently bonded to form a single-layer structure of molybdenum disulfide planes, and each layer of molybdenum disulfide is connected by van der Waals forces. The layered structure has a high specific surface area and will have a high sensitivity and selectivity when used as a gas sensor.[12,13] In our previous research, MoS_2 was found to be an excellent gas-sensitive material for ammonia sensors. Moreover, it was also learned that the surface morphology had a considerable effect on the adsorption of ammonia molecules.[14] In this study, we modified MoS_2 with SiO_2 to explore the gas-sensing properties of ammonia. The hydrothermal method was used to combine MoS_2 and SiO_2 into composite materials with the M–S structure (SiO_2 nanospheres completely covered by MoS_2) and the S–M structure (SiO_2 nanospheres distributed around the MoS_2 rosette). Ammonia sensors were constructed with three different sensing materials including MoS_2 and its composite materials (MoS_2/SiO_2 and SiO_2/MoS_2), and their sensing characteristics for ammonia were compared.

2. Materials and Methods

2.1 Preparation of silicon dioxide nanospheres

In this study, we used the sol-gel method to prepare the silicon dioxide nanospheres. Tetraethoxysilane [TEOS; $Si(OC_2H_5)_4$] was used as the precursor and ammonia water (NH_4OH) as the catalyst to synthesize silicon dioxide nanospheres through hydrolysis and condensation. In

the experiment, the concentrations of deionized (DI) water (1 mL), ethanol (C_2H_5OH, 100 mL), and TEOS (10 mL) were fixed, and that of NH_4OH was varied as 5, 10, and 15 ml to prepare various morphologies of SiO_2 nanospheres.

First, NH_4OH, DI water, and ethanol were mixed and magnetically stirred at 600 rpm for 10 min, and then TEOS was added to complete the preparation of SiO_2 precursor solutions. Next, SiO_2 precursor solutions were kept at 60 °C for 4 h. After cooling to room temperature, the reactant was transferred into a centrifuge tube using a dropper, centrifuged at 10000 rpm for 10 min using a centrifuge, and washed with ethanol and DI water for 3 cycles. To remove by-products and impurities, the centrifuged product was placed in a petri dish and baked at 80 °C for 8 h. After the water vapor was removed, the preparation of SiO_2 nanospheres was completed. The preparation process is shown in Fig. 1.

2.2   Preparation of composite materials of MoS_2 and SiO_2 nanospheres

To prepare the composites of MoS_2 and SiO_2 nanospheres, SiO_2 nanospheres with the various morphologies described above were coated in advance with sodium dodecyl benzene sulfonate (SDBS), used as the surfactant, in DI water. Then, sodium molybdate dihydrate ($Na_2MoO_4 \cdot 2H_2O$) used as the molybdenum source and thioacetamide (C_2H_5NS) used as the sulfide source were added into the solution. Finally, hydrochloric acid (HCl) was added to adjust the pH of the precursors. The precursor solution underwent a composite reaction under high temperature and pressure by the hydrothermal method to form MoS_2/SiO_2 composite materials.
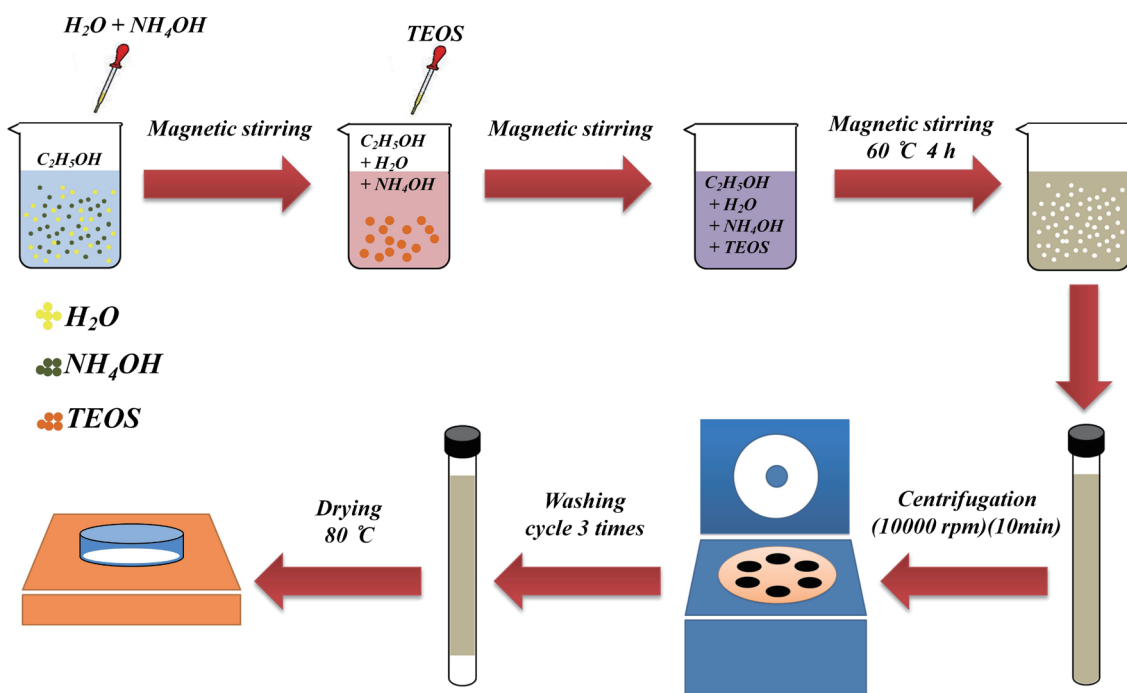

Fig. 1.   (Color online) Preparation of SiO_2 nanospheres by sol-gel method.

The preparation of composite materials is shown in Fig. 2. The obtained 70 nm or 300 nm SiO_2 nanospheres (0.05 g) and SDBS (0.05 g) were mixed with DI water (40 mL), magnetically stirred at 600 rpm for 1 h, and then $Na_2MoO_4 \cdot 2H_2O$ (0.05 M) and C_2H_5NS (0.15 M) were added. Next, the solution was adjusted to pH 5 with HCl and magnetically stirred at 600 rpm for 1 h to complete the preparation of MoS_2/SiO_2 composite precursor solutions. Then the precursor solution was poured into a 50 mL Teflon liner, placed in an autoclave, and sealed tightly. The hydrothermal reaction was carried out at 180 ℃ for 20 h. After cooling to room temperature, the reactants were poured into a centrifuge tube with a dropper, centrifuged at 10000 rpm for 10 min, and washed with ethanol and DI water for three cycles to remove by-products and impurities in the powder. Finally, the centrifuged product was placed in a petri dish and baked at 80 ℃ for 8 h. After water vapor was removed, the preparation of the MoS_2/SiO_2 composite materials was complete.

2.3   Fabrication of SAW devices

In this study, we used 128° Y-cut lithium niobate as the piezoelectric substrate of the SAW device. The IDT electrodes using aluminum metal (Al/Ti) were sputtered on the substrate using lithography technology. The thickness of the Ti metal used as an adhesion layer was 20 nm, and the thickness of the Al electrode was 100 nm. The designed parameters were a linewidth (d) of 8 μm, wavelength (λ) of 32 μm, 30 pairs of IDTs, overlap length (W) of 2.7 mm, distance (L) of the delay line area between input and output IDTs of 3 mm, and reflective grating of 30 pairs. The acoustic velocity of $LiNbO_3$ was about 3992 m/s, which resulted in a resonance frequency of about 125 MHz for the SAW device. The component schematic is shown in Fig. 3.
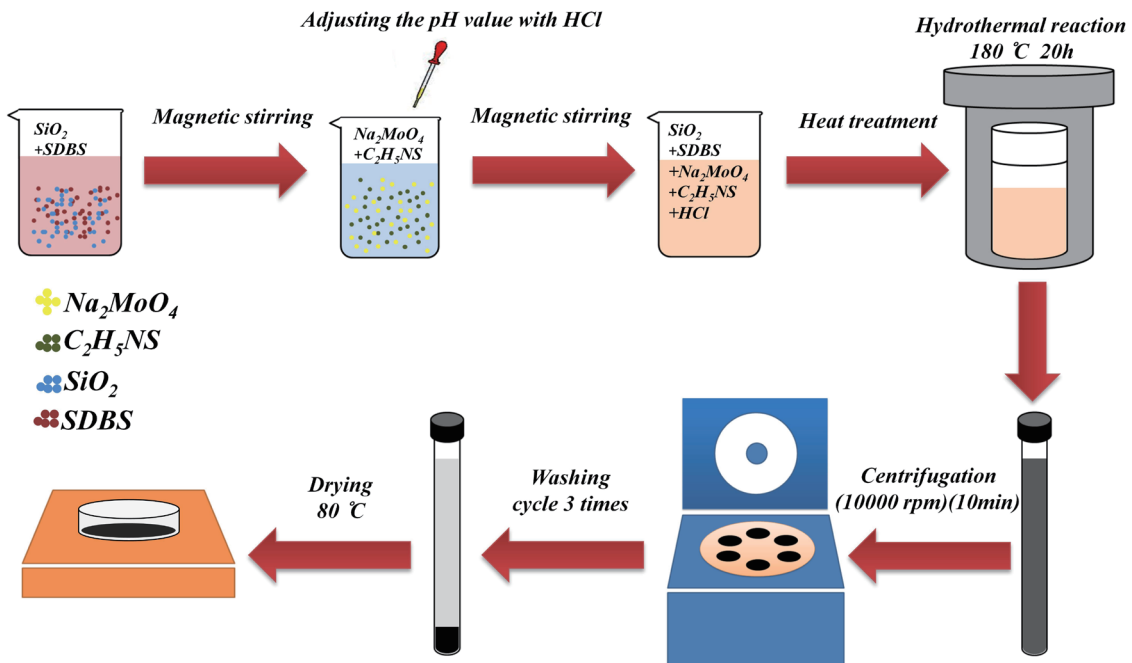

Fig. 2.   (Color online) Preparation of MoS_2/SiO_2 composite materials by hydrothermal method.
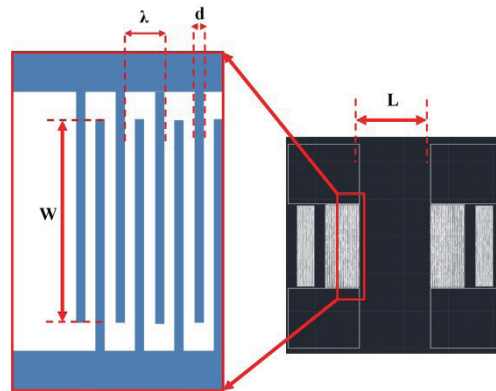
Fig. 3.   (Color online) Schematic of mask design for SAW devices.

2.4   Fabrication of SAW gas sensing devices

The preparation of a SAW gas sensor is shown in Fig. 4. The sensing material of MoS_2 or MoS_2/SiO_2 composite was fully mixed with ethanol in a weight ratio of 1:30, then the suspension was coated by spray onto the patterned delay line area through an atomizer and dried on a heating platform at 80 °C to complete the preparation of the SAW gas sensors.

Figure 5 shows the schematic of the gas sensing system. First, the gas sensing chamber and mixing chamber were pumped to a rough vacuum, then the nitrogen gas was introduced through the bubbler at a fixed flow rate to carry ammonia vapor into the mixing chamber for mixing. The Antoine equation was used to estimate the ammonia concentration.[15,16] After reaching the required gas concentration, the valve between the ammonia bubbler and the mixing chamber was closed to stop the supply of ammonia, and the valve between the mixing chamber and the sensing chamber was opened to allow gas exchange between these two chambers.

Finally, after the system reached a steady state, the frequency response of the SAW gas sensor was measured in the sensing chamber by a network analyzer. After measurement, the air extraction pump was turned on to extract the residual air inside the chamber, and nitrogen gas was introduced to clean the chamber and repeat the other measurements.

3.   Results and Discussion

3.1   Characteristics of the designed SAW device

The frequency response of the completed SAW device was measured with a network analyzer in air at room temperature. The measured center frequency of the component without coating of the sensing layer was approximately 123 MHz with a return loss (S_{11}) of −13 dB and an insertion loss (S_{21}) of −14 dB, as shown in Fig. 6.
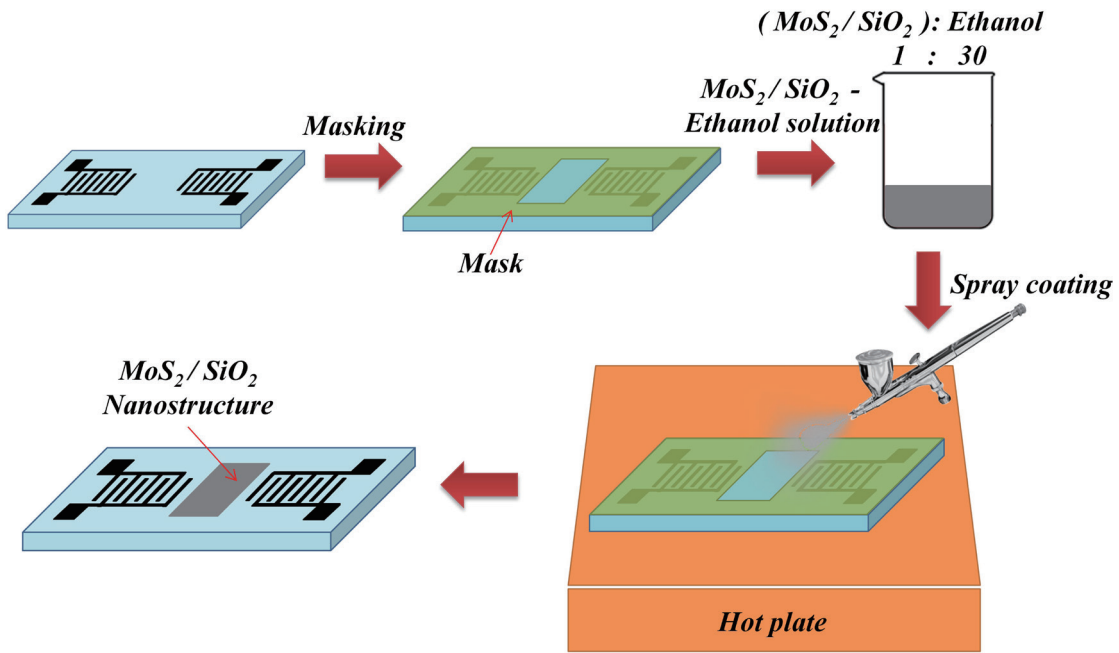
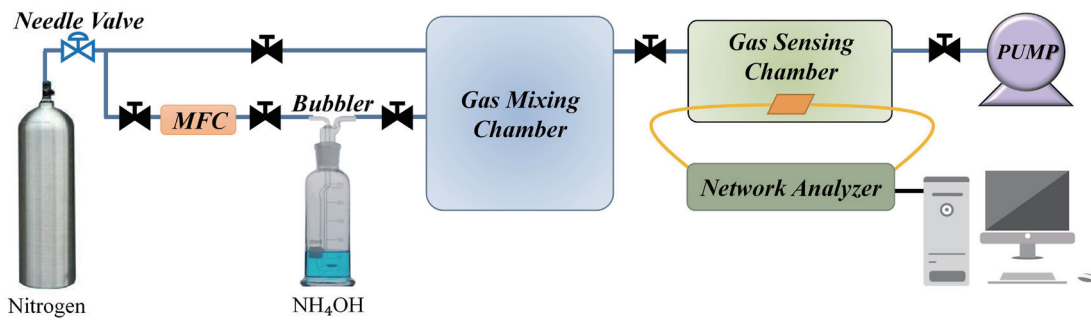Fig. 4.   (Color online) Preparation of a SAW gas sensor.

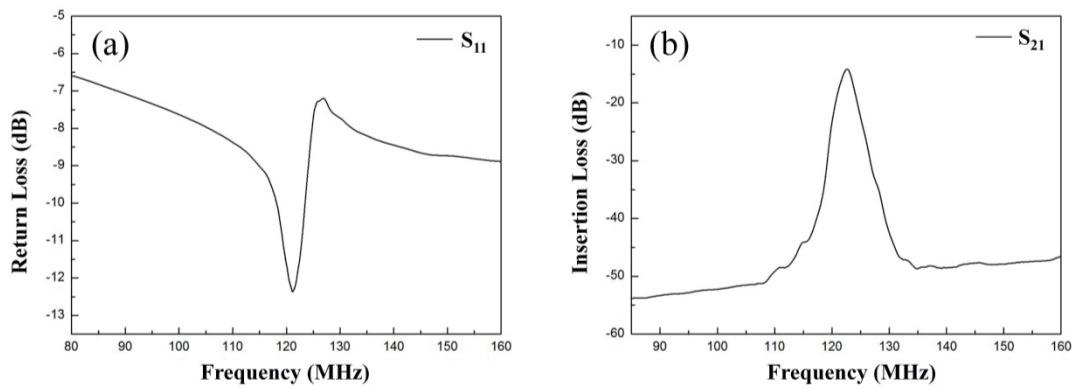Fig. 5.   (Color online) Schematic of the gas sensing system.

Fig. 6.   S parameters of the SAW device: (a) S_{11} and (b) S_{21}.

3.2 Characteristic analysis of silicon dioxide

It was found that the contents of NH_4OH in the precursors will affect the particle sizes of SiO_2 nanospheres. As ethanol of 100 mL and TEOS of 10 mL were fixed in the precursors, the morphologies of the obtained SiO_2 with various amounts of NH_4OH catalyst are shown in Fig. 7. The particle sizes of the SiO_2 nanospheres prepared with NH_4OH of 5, 10, and 15 mL were 70, 200, and 300 nm, respectively.

The EDS elemental analysis showed that the atomic ratio of oxygen to silicon was close to 2:1 for the three morphologies of SiO_2. The XRD diffraction patterns indicated that the three morphologies of SiO_2 nanospheres had only wide diffractions and behaved as amorphous forms, as shown in Fig. 8, similarly to those described in the literature.[17] In addition, the TEM analysis for SiO_2 nanospheres of 70 nm size also revealed that the SiO_2 nanospheres synthesized by the sol-gel method were amorphous, as shown in Fig. 9.
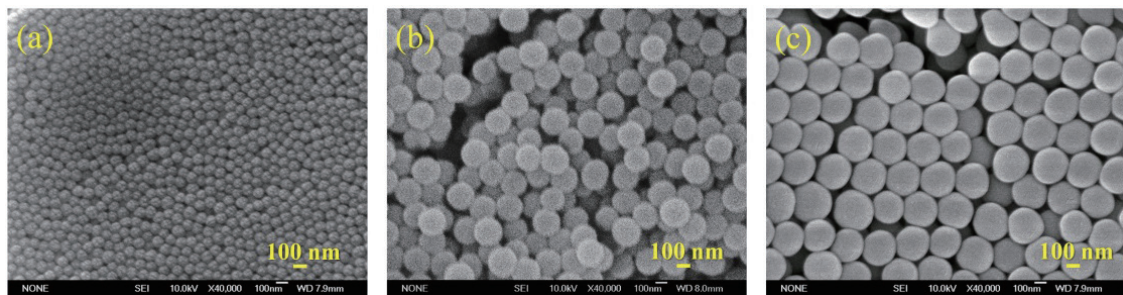

Fig. 7.   (Color online) Morphologies of SiO_2 nanospheres prepared with various amounts of NH_4OH: (a) 5, (b) 10, and (c) 15 mL.
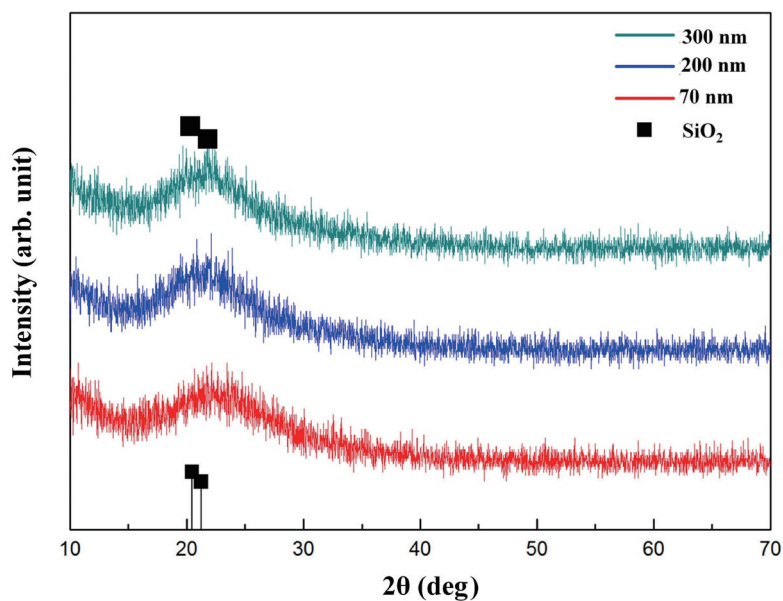

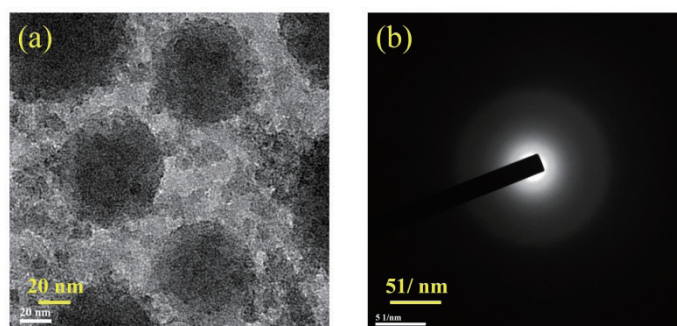Fig. 8.   (Color online) XRD diffraction patterns of SiO_2.

Fig. 9.   (Color online) TEM analysis of SiO_2 nanospheres with particle size of 70 nm: (a) HRTEM image and (b) diffraction pattern.

3.3   Characteristic analysis of molybdenum disulfide and composite materials

To prepare pure MoS_2 nanospheres, Na_2MoO_4 (0.05 M) and C_2H_5NS (0.15 M) were used as the molybdenum and sulfur sources, respectively, and the precursor was adjusted to a pH of 5 using HCl. By referring to our previous report,[14] the MoS_2 with rose morphology was obtained using the hydrothermal method, as shown in Fig. 10(a).

The composite materials using MoS_2 nanospheres and SiO_2 nanospheres with particle sizes of 70 and 300 nm, respectively, were obtained, as described above. The SEM surface morphologies revealed that the composite material synthesized with SiO_2 nanospheres with a particle size of 300 nm showed that the SiO_2 nanospheres were completely covered by MoS_2, as shown in Fig. 10(b); this will be referred as the M–S structure. On the other hand, the composite material synthesized with SiO_2 nanospheres with a particle size of 70 nm showed that the SiO_2 nanospheres were distributed around the MoS_2 rosette morphology, as shown in Fig. 10(c); this will be referred as the S–M structure.

The crystalline structure of pure MoS_2 nanospheres was analyzed by TEM, as shown in Fig. 11. Figure 11(b) shows the area selected for further HRTEM analysis, from which it was found that the MoS_2 nanospheres were in sheet form, stacked with the lattice spacing of about 0.65 nm, which is consistent with the literature[18] and corresponds to the (002) crystal plane of the MoS_2 hexagonal crystal system. In addition, Fig. 11(c) shows the diffraction patterns resulting from the MoS_2 fast Fourier transform (FFT) mode [region shown in Fig. 11(b)], from which it can be confirmed that the polycrystalline MoS_2 nanospheres prepared by the hydrothermal method were composed of many nanosheets.

Figures 12 and 13 show the EDS mappings of the elemental analysis of composite materials for the M–S and S–M structures, respectively. Figure 12 shows that the composite material with the M–S structure was composed of Mo, S, Si, and O, and the SiO_2 nanospheres were wrapped in MoS_2 nanospheres. On the other hand, Fig. 13 shows that the S–M structure was also composed of Mo, S, Si, and O, but the SiO_2 nanospheres were distributed around the periphery of MoS_2 nanospheres. Through the EDS mapping analysis, the composition and distribution of elements can be more clearly confirmed.
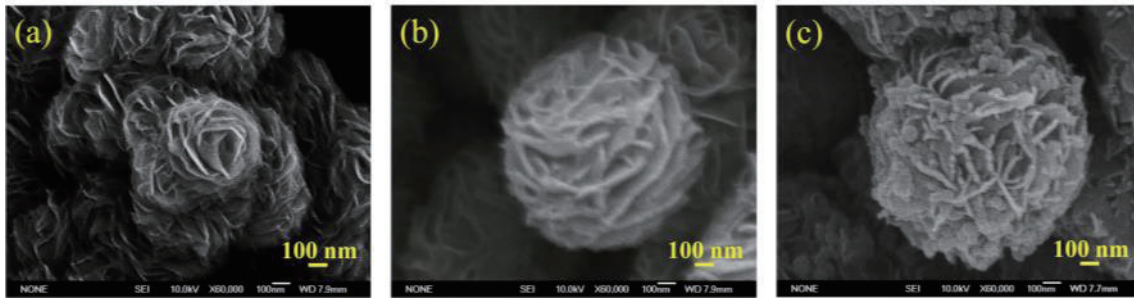
Fig. 10.   (Color online) SEM surface morphologies of the sensing materials: (a) pure MoS_2, (b) composite material with M–S structure, and (c) composite material with S–M structure.
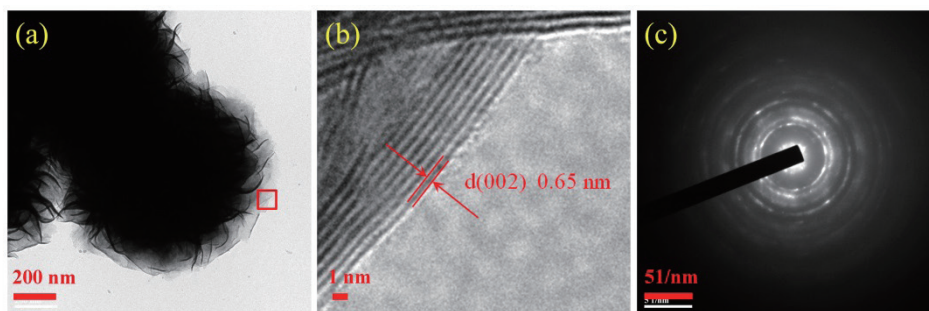

Fig. 11.   (Color online) TEM images of MoS_2 nanospheres: (a) low-magnification TEM image, (b) HRTEM image, and (c) FFT diffraction patterns.
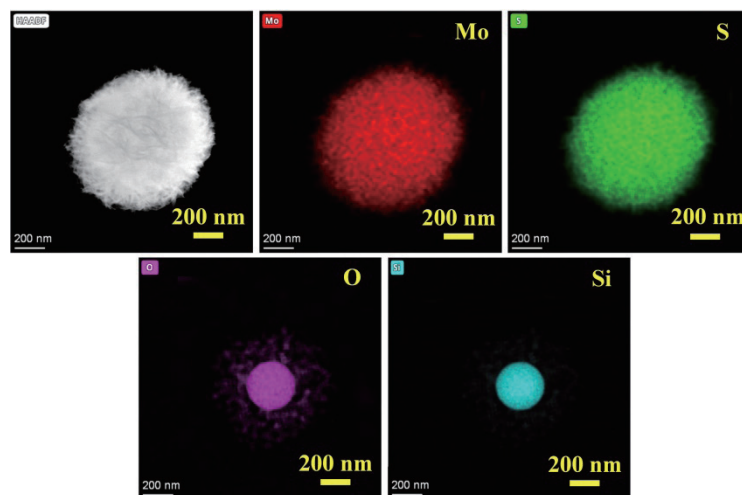

Fig. 12.   (Color online) EDS mappings of elemental analysis for composite material with M–S structure.
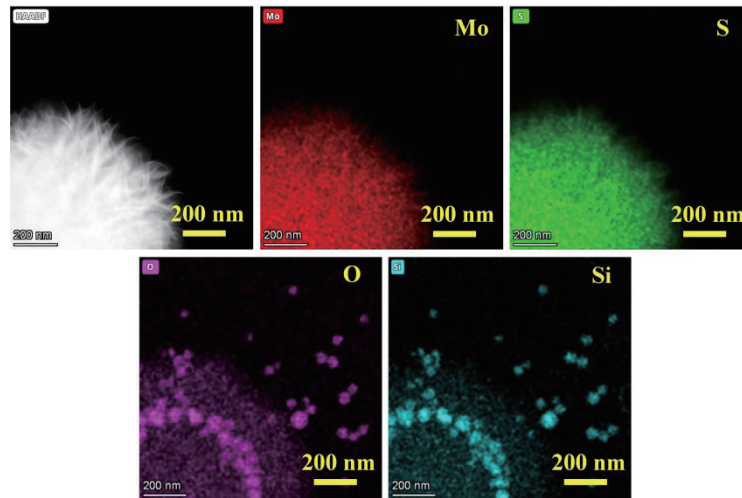
Fig. 13.　(Color online) EDS mappings of elemental analysis for composite material with S–M structure.

Figure 14 shows the XRD patterns of MoS_2 and SiO_2/MoS_2 nanocomposite materials. The XRD peaks at $2\theta = 14.2$, 32.8, 39.6, and 58.5° were indexed to be the (002), (100), (101), and (112) planes of the MoS_2 nanospheres with a tetragonal structure. It was revealed that both M–S and S–M structures of composite materials exhibit MoS_2 and SiO_2 diffraction peaks. In addition, in the X-ray diffraction analysis of the S–M structure, it was found that, except for the (002) main crystalline phase of MoS_2, other crystalline phases were affected by the decorated SiO_2 nanospheres on the surfaces of MoS_2, and the diffraction intensity was weak compared with those of pure MoS_2 and M–S structures.

Figure 15 shows the BET analysis results of MoS_2 and composite materials with M–S and S–M structures. From the adsorption and desorption characteristic curves, the specific surface areas can be calculated to be 30.48, 32.59, and 115.57 m^2/g for pure MoS_2, the M–S structure, and the S–M structure, respectively. The results indicated that the composite material with the S–M structure had a much higher specific surface area and optimal adsorption and desorption characteristics.

3.4　Analysis of ammonia gas sensor

The SAW gas sensors sprayed with MoS_2 and composite materials with the M–S and S–M structures on the delay line areas were denoted as Sensor-A, Sensor-B, and Sensor-C, respectively. The frequency responses at different ammonia concentrations for the three sensors are shown in Figs. 16–18, respectively.

The resonance center frequency of all sensors with sensing materials coated and without NH_3 gas was approximately 122 MHz. As the NH_3 gas concentration increased, the sensors shifted to lower frequencies. The frequency shifts of the three gas sensors with NH_3 gas concentration are shown in Fig. 19. The sensitivity can be calculated as follows.
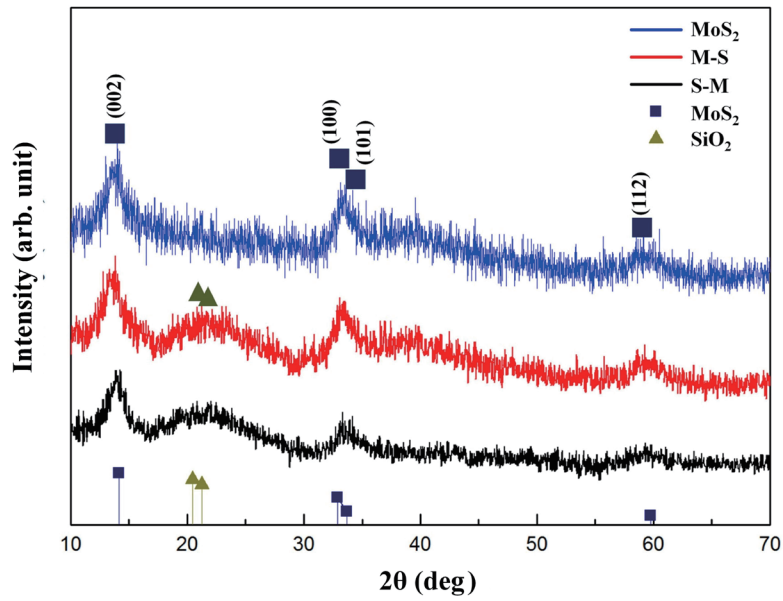
Fig. 14.   (Color online) XRD diffractions of MoS$_2$ and SiO$_2$/MoS$_2$ composite materials.
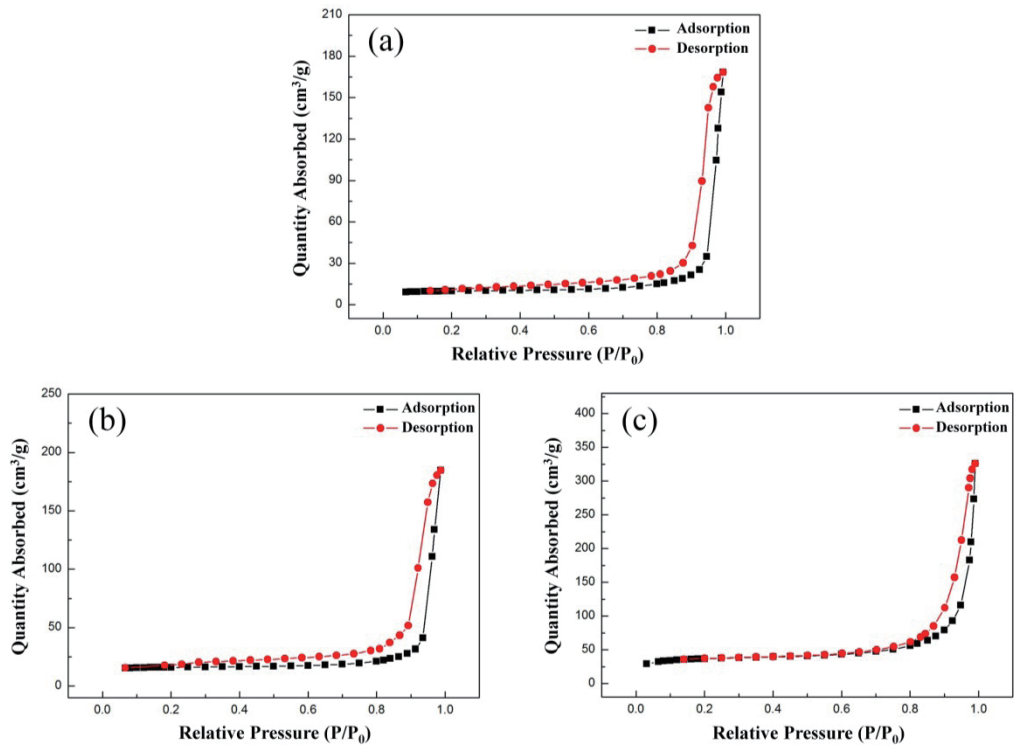
Fig. 15.   (Color online) BET analysis results of MoS$_2$ and composite materials with M–S and S–M structures: (a) pure MoS$_2$, (b) composite material with M–S structure, and (c) composite material with S–M structure.

(a)　　　　　　　　　　　　　(b)

Fig. 16.　(Color online) (a) Frequency variations of Sensor-A at different ammonia concentrations. (b) Enlargement around the center frequency of 122 MHz.

(a)　　　　　　　　　　　　　(b)

Fig. 17.　(Color online) (a) Frequency variations of Sensor-B at different ammonia concentrations. (b) Enlargement around the center frequency of 122 MHz.

(a)　　　　　　　　　　　　　(b)

Fig. 18.　(Color online) (a) Frequency variations of Sensor-C at different ammonia concentrations. (b) Enlargement around the center frequency of 122 MHz.

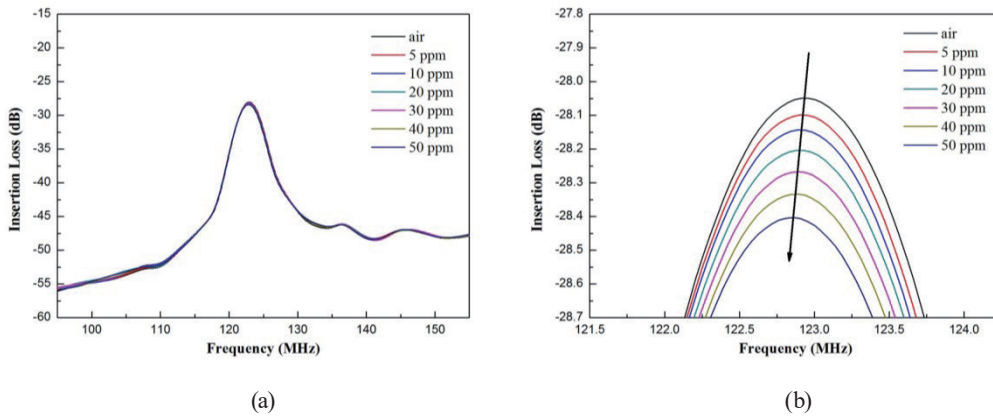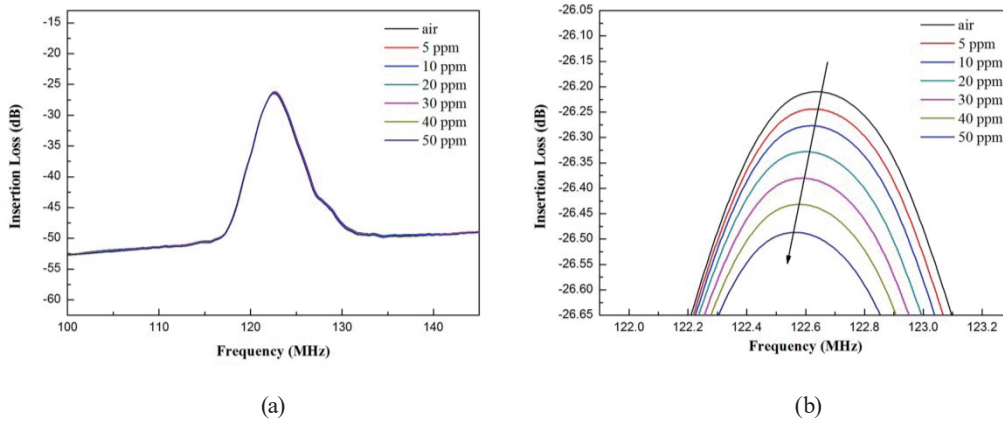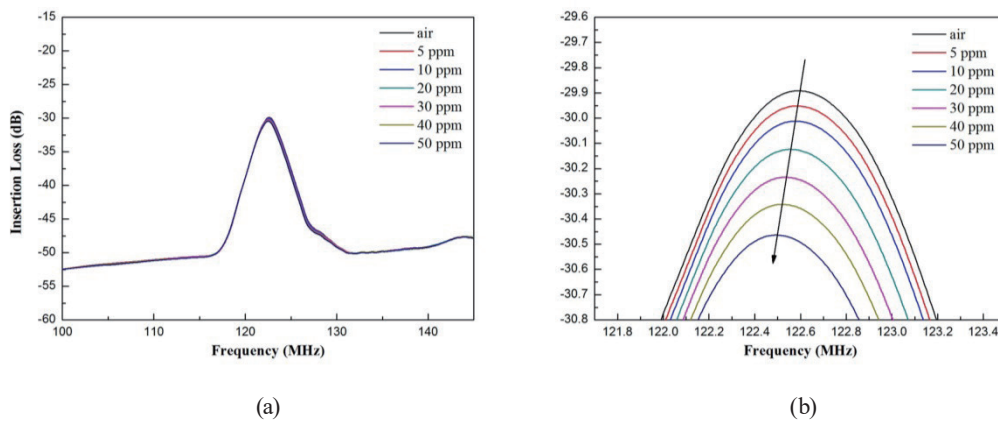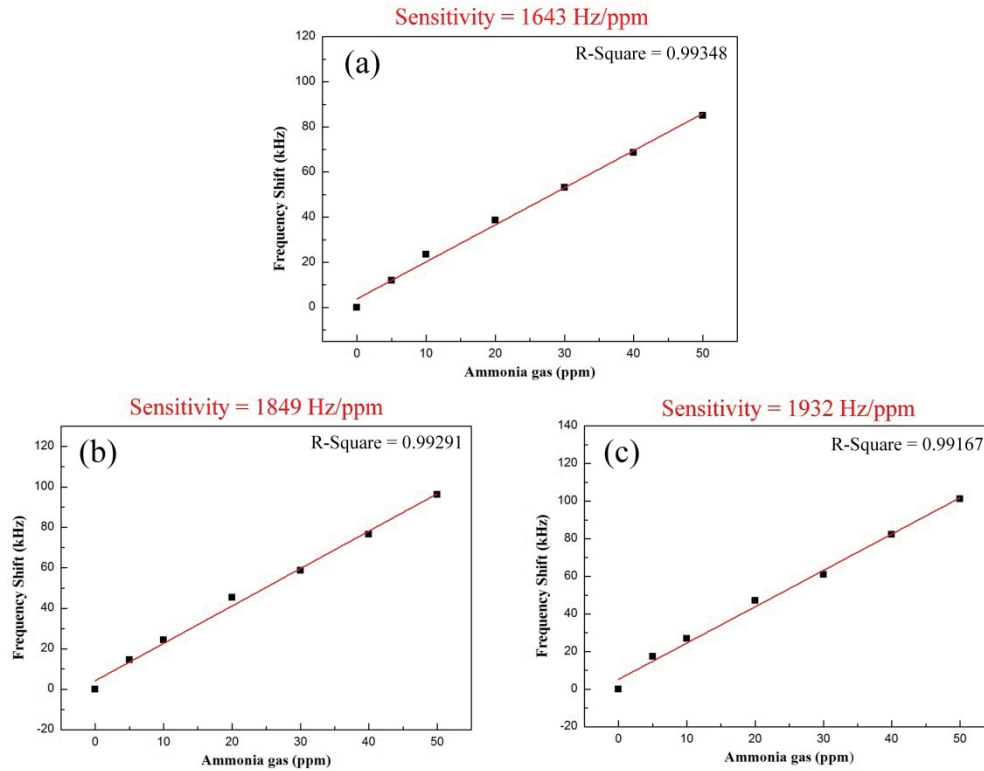Fig. 19.   (Color online) Frequency shifts of sensors with NH_3 gas concentration: (a) Sensor-A, (b) Sensor-B, and (c) Sensor-C.

$$S\left(\text{Hz / ppm}\right) = \frac{\left|f_{air} - f_{gas}\right|}{\Delta c} \qquad (1)$$

Here, S is the sensitivity with the unit of Hz/ppm, f_{air} is the frequency of the sensor in air, f_{gas} is the frequency at which ammonia gas is detected, and ΔC is the change in gas concentration. According to Eq. (1), the sensitivities of Sensor-A, Sensor-B, and Sensor-C were calculated to be 1643, 1849, and 1932 Hz/ppm, respectively.

In a SAW gas sensor, the center frequency shift (Δf) may be related to elastic or acoustic-electrical interactions of the sensing material or to the mass load changes due to the adsorption of gas molecules.[19] However, the elastic change of the sensing material will cause the center frequency to move to the higher end (the material becomes stiffer, which will increase the center frequency). That is, the material elasticity can be ruled out and its effects ignored[20] because the frequency shifts to the lower end in this experiment.

The acoustic and electrical effects on the gas sensor can be expressed using the following formula.[20]

$$\Delta f = -f_0 \times \frac{k^2}{2} \times \left(\cfrac{1}{1 + \left(\cfrac{V_0 C_s}{\sigma_s} \right)^2} \right) \qquad (2)$$

f_0 is the unperturbed center frequency of the sensor, V_0 is the unperturbed SAW velocity of about 3992 m/s of the SAW device on an $LiNbO_3$ substrate, σ_s is the conductivity of the sensing layer, f_0 is the center frequency of the sensor, k^2 is the electromechanical coupling coefficient, and C_s is the unit length capacitance of the SAW device. Since MoS_2 is an *n*-type semiconductor, as it is exposed to ammonia gas, the number of electrons in the conduction band of MoS_2 will increase[21] owing to the electron-donating characteristics of ammonia molecules,[22] and the conductivity of the material increases,[19] which will result in an electrical load effect and cause the center frequency of the device to shift to the lower end.

Furthermore, it must be noted that mass loading will cause the center frequency to shift toward the lower end (i.e., lower the center frequency). From the results obtained, it can be concluded that the frequency shift is mainly due to the mass loading effect. The surface of silicon dioxide (SiO_2) contains a rich amount of hydroxyl groups (–OH) because, when it encounters water molecules, a chemical reaction occurs that produces hydroxyl groups.[23] Since SiO_2 is rich in hydroxyl groups (–OH), the N atoms or H atoms in NH_3 can form hydrogen bonds with the (–OH) groups in SiO_2. Moreover, so SiO_2 has a strong water absorption capacity, which is beneficial to highly water-soluble NH_3 sensing.

The mass loading effect of the gas sensor can be expressed as follows.[24,25]

$$\Delta f = (k_1 + k_2) \times f_0^2 \times \Delta \rho s \qquad (3)$$

Here, k_1 (-3.775×10^{-8} m^2 s kg^{-1}) and k_2 (-1.73×10^{-8} m^2 s kg^{-1}) are the material constants of the 128° Y-cut $LiNbO_3$ substrate. Note here that k_1 and k_2 are both negative values, so a positive change in $\Delta \rho s$ will lead to a negative value of Δf, resulting in a shift of the center frequency to a lower frequency.[26,27]

In this study, Sensor-C, with an S–M structured composite material as the sensing layer, showed the best performance as an ammonia sensor. The reason may be that MoS_2 has a nanoflower shape with a high specific surface area decorated with SiO_2 nanospheres with hydroxyl-rich characteristics and high specific surface area, which will provide many more active sites to adsorb ammonia molecules and obtain higher sensing performance[28,29] than other sensors.

The selectivity of gas sensing for the three gas sensors was analyzed for sensing acetone, ethanol, and toluene gases. The sensing temperatures were all room temperature, and the concentration of each gas was 50 ppm. The results are shown in Fig. 20. From the results, it can be seen that all the sensors exhibited good selectivity. However, Sensor-C had a lower selectivity than Sensor-A and Sensor-B, although it exhibited the best sensing performance. The reason may be that the (–OH) hydroxyl group in SiO_2 forms hydrogen bonds not only with NH_3, but
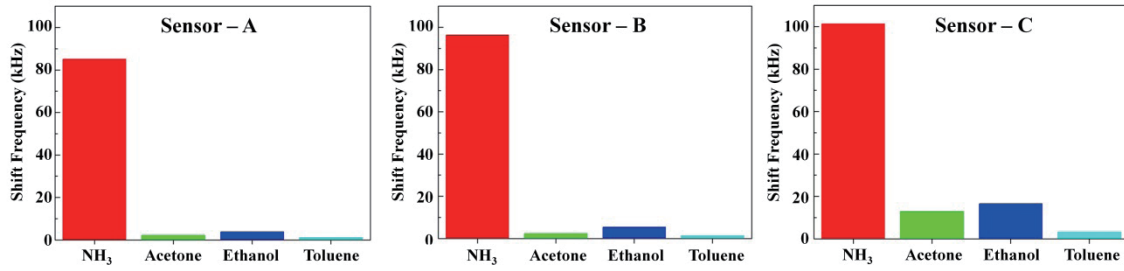
Fig. 20.   (Color online) Sensing selectivities of the three gas sensors to different gases.

also with acetone and alcohol. Compared with Sensor-A and Sensor-B, the response of Sensor-C to acetone and alcohol was higher.

Finally, three sets of gas sensing devices were used to determine their dynamic gas sensing characteristics at room temperature with an ammonia concentration of 50 ppm. The phase variations of the center frequency were observed, and the response time and recovery time were determined using a network analyzer (P9372A Keysight streamline USB Vector Network). During the measurement, ammonia gas with a concentration of 50 ppm was first introduced into the sensing chamber and then the phase shift of the center frequency was recorded. After the phase shift stabilized, the ammonia gas in the cavity was pumped out, and the phase angle of the center frequency returned to its initial state. As the phase angle decreased and rose by 90%, durations were recorded as the response time and recovery time, respectively.

Figure 21 shows the results of the three sensors. The response times were found to be 32, 30, and 21 s, whereas the recovery times were 32, 30, and 23 s for Sensor-A, Sensor-B, and Sensor-C. Phase can be converted to frequency according to Eqs. (4) and (5).

$$\frac{\left|\theta_{air} - \theta_{gas}\right|}{\theta_{air}} \times 100\% = \Delta\theta \tag{4}$$

$$f_{air} \times \Delta\theta = \Delta f \tag{5}$$

Here, θ_{air} is the phase angle of the center frequency in air, θ_{gas} is the phase angle of the center frequency in an atmosphere with 50 ppm ammonia, $\Delta\theta$ is the percentage of phase angle displacement, and Δf is the frequency displacement. The change in phase angle can be converted into a change in frequency through the above formulas (see Table 1). The values of Δf in Table 1 were close to those obtained in Fig. 19. Sensor-C was used to perform continuous dynamic sensing with ammonia gas at concentrations of 5–50 ppm. As shown in Fig. 22, the results exhibit an excellent sensing linearity with an R-squared value of about 0.99167.

Finally, compared with other works in the literature, the ammonia gas sensor we prepared in this study showed excellent sensitivity, response time, and recovery time,[30–34] as shown in Table 2.
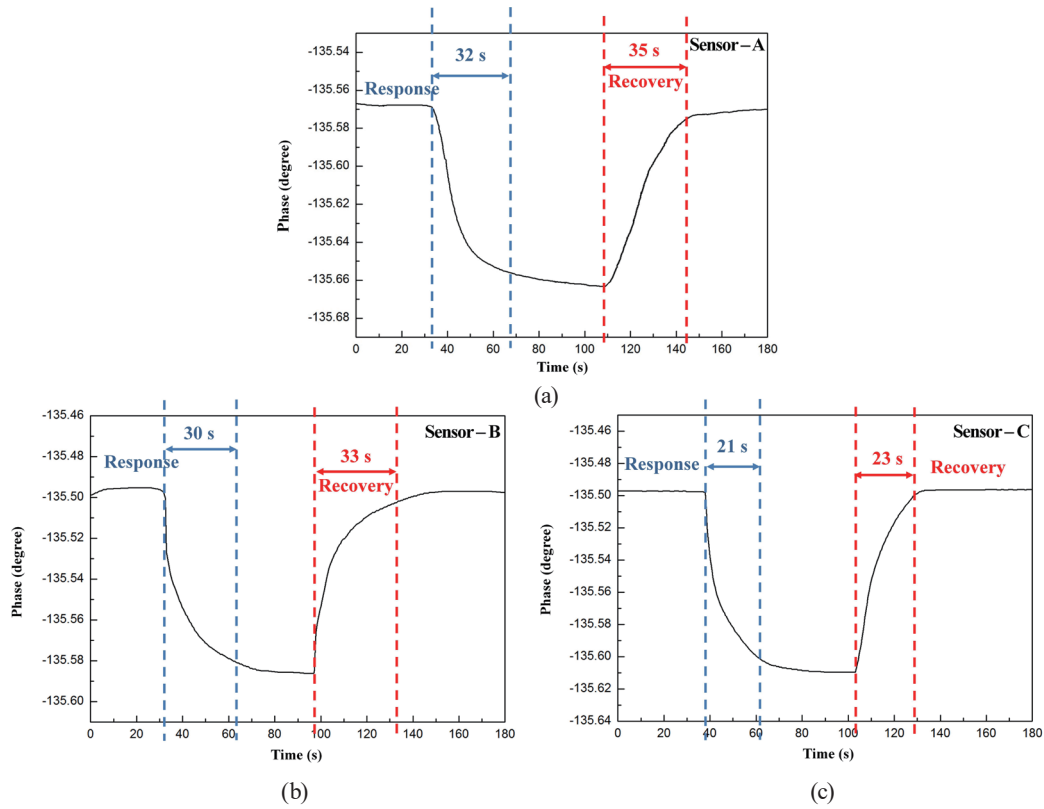
Fig. 21. (Color online) Dynamic response characteristics of each sensor: (a) Sensor-A, (b) Sensor-B, and (c) Sensor-C.

Table 1
Phase angle displacement and converted frequency shift of three gas sensors at 50 ppm ammonia gas.

Sensor number	θ_{air} (°)	θ_{gas} (°)	f_{air} (Hz)	Δf (kHz)
A	135.5678	135.6616	122.941326	85.064
B	135.4949	135.6013	122.652542	96.315
C	135.4979	135.6098	122.597988	101.246

Fig. 22. (Color online) Dynamic response of Sensor-C to NH_3 gas of 5–50 ppm.

Table 2
SAW ammonia sensor performance.

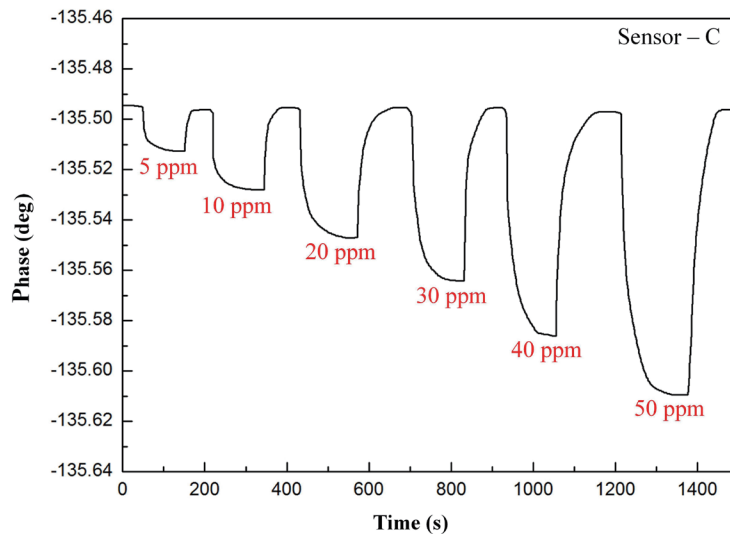| Working Frequency (MHz)	Sensing Material	Sensitivity (Hz/ppm)	Response and Recovery times	Ref.
200	SiO_2/TiO_2	2000	75 s and 140 s (in 40 ppm)	[30]
200	SiO_2/SnO_2	210	220 s and 240 s (in 40 ppm)	[31]
200	TiO_2	500	45 s and 125 s (in 50 ppm)	[32]
200	ZnO/SiO_2	113.2	80 s and 80 s (in 50 ppm)	[33]
200	ZnS	190	40 s and 80 s (in 20 ppm)	[34]
123	MoS_2/SiO_2	1932	21 s and 23 s (in 50 ppm)	Present work

4.   Conclusions

In this study, we successfully prepared a delay line SAW element with a center frequency of approximately 123 MHz using a 128° Y-cut $LiNbO_3$ piezoelectric substrate. The sensing materials of pure MoS_2 and composites with the MoS_2–SiO_2 (M–S) structure and the SiO_2–MoS_2 (S–M) structure were sprayed on the delay line areas of the SAW devices as the NH_3 gas sensors.

By adjusting the amount of catalyst NH_4OH in the precursors, the particle sizes of SiO_2 nanospheres were successfully controlled at 70, 200, and 300 nm by the sol-gel method. Then, SiO_2 nanospheres were added to the precursor to prepare the rosette-shaped MoS_2, and nanocomposites were synthesized by the hydrothermal method. Through EDS mapping of elemental analysis, we found that the MoS_2–SiO_2 (M–S) structure can be synthesized using 300 nm SiO_2 nanospheres completely covered by MoS_2. The SiO_2–MoS_2 (S–M) structure can be synthesized using 70 nm SiO_2 nanospheres, which were distributed around MoS_2 flower spheres. Through the BET analysis, it was revealed that the composite material with the S–M structure had the highest specific surface area of 115.57 m^2/g with optimized adsorption and desorption characteristics.

The SAW gas sensors fabricated using MoS_2 and composite materials with the M–S and S–M structures were denoted as Sensor-A, Sensor-B, and Sensor-C, respectively. The sensitivities of Sensor-A, Sensor-B, and Sensor-C were determined to be 1643, 1849, and 1932 Hz/ppm, respectively. All three sensors have good selectivity; however, Sensor-C had a lower selectivity than Sensor-A and Sensor-B. The reason may be that the (–OH) hydroxyl group in SiO_2 will form hydrogen bonds not only with NH_3, but also with acetone and alcohol. By the dynamic response measurement, it was found that the response times were 32, 30, and 21 s, for Sensor-A, Sensor-B, and Sensor-C, whereas the recovery times were 35, 33, and 23 s, respectively. A sensing linearity with an R-squared value of about 0.99167 was obtained for Sensor-C through continuous dynamic sensing with ammonia gas concentrations of 5–50 ppm. Finally, in this study, we discovered that composite materials with special M–S and S–M structures were synthesized from SiO_2 with different particle sizes and successfully revealed that modifying MoS_2 with SiO_2 nanospheres improved the adsorption of ammonia molecules and significantly increased the sensitivity of the sensor.

References

1   A. Clappier, P. Thunis, M. Beekmann, J. Putaud, and A. De Meij: Environ. Int. l **156** (2021) 106699. https://doi.org/10.1016/j.envint.2021.106699

2   Y. Zhou, X. Li, Y. Wang, H. Tai, and Y. Guo: Anal. Chem. **91** (2018) 3311. https://doi.org/10.1021/acs.analchem.8b04347

3   D. Zhang, Z. Yang, P. Li, M. Pang, and Q. Xue: Nano Energy **65** (2019) 103974. https://doi.org/10.1016/j.nanoen.2019.103974

4   A. Kumar, A. Sanger, A. Kumar, and R. Chandra: RSC Adv. **6** (2016) 77636. https://doi.org/10.1039/C6RA14342C

5   B. de Lacy Costello, A. Amann, H. Al-Kateb, C. Flynn, W. Filipiak, T. Khalid, D. Osborne, and N. M. Ratcliffe: J. Breath Res. **8** (2014) 014001. https://doi.org/10.1088/1752-7155/8/1/014001

6   A. Mirzaei, S. S. Kim, and H. W. Kim: J. Hazard. Mater. **357** (2018) 314. https://doi.org/10.1016/j.jhazmat.2018.06.015

7   P. K. Basu, S. Benedict, S. Kallat, and N. Bhat: J. Microelectromech. Syst. **26** (2016) 48. https://doi.org/10.1109/JMEMS.2016.2636333

8   X. Chen, S. Zhao, P. Zhou, B. Cui, W. Liu, D. Wei, and Y. Shen: Sens. Actuators, B **328** (2021) 129070. https://doi.org/10.1016/j.snb.2020.129070

9   L. Rana, R. Gupta, M. Tomar, and V. Gupta: Sens. Actuators, B **252** (2017) 840. https://doi.org/10.1016/j.snb.2017.06.075

10   S.-H. Wang, C.-Y. Shen, Z.-J. Lien, and J.-H. Wang: Sens. Actuators, B **243** (2017) 1075. https://doi.org/10.1016/j.snb.2016.12.101

11   L. Rana, R. Gupta, R. Kshetrimayum, M. Tomar, and V. Gupta: Surf. Coat. Technol. **343** (2018) 89. https://doi.org/10.1016/j.surfcoat.2017.10.077

12   R. K. Chava, J. Y. Do, and M. Kang: Appl. Surf. Sci. **433** (2018) 240. https://doi.org/10.1016/j.apsusc.2017.09.260

13   T. Järvinen, G. S. Lorite, J. Peräntie, G. Toth, S. Saarakkala, V. K. Virtanen, and K. Kordas: Nanotechnology **30** (2019) 405501. https://doi.org/10.1088/1361-6528/ab2d48

14   C.-Y. Chung, Y.-C. Chen, F.-R. Juang, K.-S. Kao, and E.-I. Lee: Materials **16** (2023) 4703. https://doi.org/10.3390/ma16134703

15   T. Boublík, V. Fried, and E. Hála: The Vapour Pressures of Pure Substances (Elsevier Science Publishers, New York, 1984) 2nd ed.

16   M. Doble: Perry's Chemical Engineers' Handbook (McGraw-Hil, New York, 2007) 8th ed.

17   N. D. Singho, and M. R. Johan: Int. J. Electrochem. Sci. **7** (2012) 5604.

18   B. Radisavljevic, A. Radenovic, J. Brivio, V. Giacometti, and A. Kis: Nat. Nanotechnol. **6** (2011) 147. https://doi.org/10.1038/nnano.2010.279

19   D. Ballantine Jr, R. M. White, S. J. Martin, A. J. Ricco, E. Zellers, G. Frye, and H. Wohltjen: Acoustic Wave Sensors Theory, Design and Physico-chemical Applications (Academic Press, Milwaukee, 1996) 1st ed.

20   D. Morgan: Surface Acoustic Wave Filters with Applications to Electronic Communications and Signal Processing (Elsevier Science, New York, 2010) 2nd ed.

21   B. Liu, L. Chen, G. Liu, A.N. Abbas, M. Fathi, and C. Zhou: ACS Nano **8** (2014) 5304. https://doi.org/10.1021/nn5015215

22   B. Cho, M. G. Hahm, M. Choi, J. Yoon, A. R. Kim, Y.-J. Lee, S.-G. Park, J.-D. Kwon, C. S. Kim, and M. Song: Sci. Rep. **5** (2015) 8052. https://doi.org/10.1038/srep08052

23   T. Parrill: J. Mater. Res. **7** (1992) 2230. https://doi.org/10.1557/JMR.1992.2230

24   A. Ricco, S. Martin, and T. Zipperian: Sens. Actuators **8** (1985) 319. https://doi.org/10.1016/0250-6874(85)80031-7

25   M. Penza, P. Aversa, G. Cassano, W. Wlodarski, and K. Kalantar-Zadeh: Sens. Actuators, B **127** (2007) 168. https://doi.org/10.1016/j.snb.2007.07.028

26   Y.-L. Tang, Z.-J. Li, J.-Y. Ma, H.-Q. Su, Y.-J. Guo, L. Wang, B. Du, J.-J. Chen, W. Zhou, and Q.-K. Yu: J. Hazard. Mater. **280** (2014) 127. https://doi.org/10.1016/j.jhazmat.2014.08.001

27   D. Burman, H. Raha, B. Manna, P. Pramanik, and P. K. Guha: ACS Sens. **6** (2021) 3398. https://doi.org/10.1021/acssensors.1c01258

28   W. Wang, Y. Zhen, J. Zhang, Y. Li, H. Zhong, Z. Jia, Y. Xiong, Q. Xue, Y. Yan, and N. S. Alharbi: Sens. Actuators, B **321** (2020) 128471. https://doi.org/10.1016/j.snb.2020.128471

29   L. Wenbo, Q. Rong, Z. Shangjun, J. Hong, S. Cheng, and Z. Yueqin: Int. J. Inorg. Mater. **37** (2022) 1135. https://doi.org/10.15541/jim20220053

30 Y. Tang, D. Ao, W. Li, X. Zu, S. Li, and Y. Q. Fu: Sens. Actuators, B **254** (2018) 1165. https://doi.org/10.1016/j.snb.2017.07.195

31 Y. Guo, G. Long, Y. Tang, J. Wang, Q. Tang, X. Zu, J. Ma, B. Du, H. Torun, and Y. Fu: Smart Mater. Struct. **29** (2020) 095003. https://doi.org/10.1088/1361-665X/ab9e06

32 L. Zhao, R. Wang and Q. Cao: Sens. Mater. **32** (2020) 4111. https://doi.org/10.18494/SAM.2020.3189

33 S.-Y. Wang, J.-Y. Ma, Z.-J. Li, H. Su, N. Alkurd, W.-L. Zhou, L. Wang, B. Du, Y.-L. Tang, and D.-Y. Ao: J. Hazard. Mater. **285** (2015) 368. https://doi.org/10.1016/j.jhazmat.2014.12.014

34 G. Long, Y. Guo, W. Li, Q. Tang, X. Zu, J. Ma, B. Du, and Y. Fu: Microelectron. Eng. **222** (2020) 111201. https://doi.org/10.1016/j.mee.2019.111201